Magnetic properties of the α-T_3 model: Magneto-optical conductivity and the Hofstadter butterfly

E. Illes* and E. J. Nicol
Department of Physics, University of Guelph, Guelph, Ontario, Canada N1G 2W1
and Guelph-Waterloo Physics Institute, University of Guelph, Guelph, Ontario, Canada N1G 2W1
(Received 30 May 2016; revised manuscript received 25 August 2016; published 23 September 2016)

The α-T_3 model interpolates between the pseudospin $S = 1/2$ honeycomb lattice of graphene and the pseudospin $S = 1$ dice lattice via parameter α. We present calculations of the magnetic properties of this hybrid pseudospin model, namely the absorptive magneto-optical conductivity and the Hofstadter butterfly spectra. In the magneto-optics curves, signatures of the hybrid system include a doublet structure present in the peaks, resulting from differing Landau level energies in the K and K' valleys. In the Hofstadter spectra, we detail the evolution of the Hofstadter butterfly as it changes its periodicity by a factor of three as we vary between the two limiting cases of the α-T_3 model.

DOI: 10.1103/PhysRevB.94.125435

I. INTRODUCTION

Graphene, experimentally isolated in 2004 [1], is a two-dimensional sheet of carbon atoms arranged on a honeycomb lattice (HCL). Its low-energy excitations are described by the two-dimensional (2D) massless Dirac equation, or the Dirac-Weyl equation with pseudospin $S = 1/2$. In a magnetic field perpendicular to the lattice, the states of graphene condense into Landau levels (LLs) with energies proportional to $\sqrt{B}$ for both electrons and holes [2]. These LLs include a zero-energy LL with both electron and hole character, resulting in a half-integer anomalous Hall effect [3–5].

Modifying the HCL by coupling one of the two inequivalent sites of the HCL to an additional atom located at the center of each hexagon yields the T_3 or dice lattice [6–8]. This lattice could be naturally formed by growing a trilayer structure of cubic lattices such as $SrTiO_3$/$SrIrO_3$/$SrTiO_3$ in the (111) direction [9] or by confining cold atoms to an optical lattice [10]. The low-energy behavior of the dice lattice is described by the same Dirac-Weyl Hamiltonian as graphene, but with pseudospin $S = 1$.

Allowing a parameter α to describe the strength of the coupling between the HCL and the atom at the center of each hexagon results in the α-T_3 lattice [11]. In the limit of α approaching 0 and 1, we obtain the HCL (with an inert central atom) and the dice lattice, respectively. The α-T_3 model was initially proposed for cold atoms confined to an optical lattice, and more recently, a model for $Hg_{1-x}Cd_xTe$ taken in the 2D limit at critical doping has been shown to map onto the α-T_3 model, with an intermediate value of the coupling parameter $\alpha = 1/\sqrt{3}$ [12]. The α-T_3 model is characterized by a nontopological Berry phase that varies with the parameter α [11,13]. The model has also been extended to include on-site potential terms, uniaxial compression, and a bilayer version of the α-T_3 model [14]. In contrast to graphene and the dice lattice, the α-T_3 model has LLs that form at different energies in the inequivalent K and K' valleys [11,15] for $0 < \alpha < 1$.

Magneto-optical spectroscopy [16] can be used to probe the underlying electronic structure and excitation spectra by measuring transitions between LLs. In graphene it has been used to measure the energy spacing between its unusual LL structure for single [17,18] and multilayer graphene [19,20], and to measure its electron and hole velocities. Magneto-optical conductivity has been calculated for single [21] and multilayer [22] graphene as well as the dice lattice and general pseudospin systems [23]. Here we calculate the magneto-optical conductivity for the hybrid pseudospin system that can be described as a mixture of pseudospin $S = 1/2$ and $S = 1$. We discuss the LL structure of the α-T_3 lattice such as the different LL energies in the K and K' valleys, and examine its effects on magneto-optics curves as a function of the parameter α, the magnetic field strength, and with changing chemical potential.

Charged particles moving through a periodic lattice that is subjected to a perpendicular magnetic field experience an interplay of two quantizing fields, resulting in the Hofstadter butterfly [24]. In particular, the periodicity of the lattice creates an electrostatic field that quantizes the motion of the charged particles into Bloch bands. Similarly, a magnetic field, applied perpendicular to the lattice, quantizes the energy of the electrons into highly degenerate LLs. When the length scale of these two quantizing fields is on the same order, the Bloch bands and the LLs compete to split the energy spectrum, resulting in a self-similar energy spectrum, called the Hofstadter butterfly.

Experimental observation of Hofstadter butterfly spectra requires finding a system in which the quantizing fields are able to compete on similar length scales using experimentally achievable fields. Recently, Moiré superlattices [25], which can be made from twisted graphene [26–28] or by placing graphene on a hexagonal boron nitride substrate [29–32], have offered this possibility in laboratory achievable fields. Cold atoms in an optical lattice have also been explored for this purpose [33,34].

Hofstadter butterfly spectra have been calculated for the HCL [35–39] and the dice lattice [7], which are the two limiting cases of the α-T_3 model. Here we detail the continuous evolution of the Hofstadter butterfly spectrum between these two limiting cases, and provide the difference equation required for calculating Hofstadter butterfly spectra for this intermediate regime.

The remainder of this paper is laid out as follows. In Sec. II we describe the α-T_3 model, including the Hamiltonian and

*illese@uoguelph.ca

wave functions of the model under a perpendicular magnetic field. In Sec. III we present magneto-optical conductivity curves for the α-T_3 model and highlight signatures of the hybrid pseudospin system. Section IV contains the difference equation required for calculating Hofstadter butterfly spectra for intermediate values of α and some representative spectra for this regime. Finally, our conclusions can be found in Sec. V.

II. THE α-T_3 MODEL

The α-T_3 model [11] interpolates between the pseudospin $S = 1/2$ HCL of graphene, and the pseudospin $S = 1$ dice (or T_3) lattice via parameter α. Figure 1(a) depicts the α-T_3 lattice in which sites A and B form a hexagonal lattice, and site C sits at the center of the hexagons. Hopping takes place between atoms at sites A and B with strength t, and a variable hopping of αt connects the B and C sites. Hopping between sites A and C is not permitted for this model.

Throughout this paper we will refer to the limiting case of $\alpha = 1$ as the dice lattice, and $\alpha \to 0$ as graphene, for convenience, despite some differences between graphene and the latter limit. These differences arise from the presence of the C sites, which are located at the center of each hexagon even when they are fully decoupled from the HCL (as is the case for $\alpha = 0$). The result is a three atom per unit cell problem with an inert central atom, rather than the usual two atom per unit cell problem of graphene. The intermediate regime, in which $0 < \alpha < 1$, describes a hybrid pseudospin $S = 1/2$ and pseudospin $S = 1$ system.

The low-energy spectrum for the α-T_3 lattice is shown in Fig. 1(c) and consists of the usual linearly dispersing conical bands expected for graphene, with an additional dispersionless flat band that cuts through the Dirac point. All of these bands are present and remain unchanged for the full range of α.

In this paper we are interested in the properties of the α-T_3 model in the presence of a magnetic field B that is applied

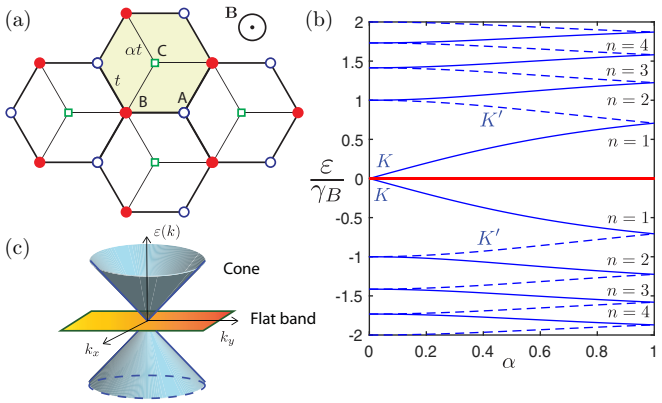

FIG. 1. (a) The α-T_3 lattice, in a perpendicular magnetic field B. Hopping between sites A and B (which form a HCL) takes place with strength t. Sites labeled C, located at the centers of the hexagons, are coupled only to B sites with variable hopping amplitude αt. (b) Landau level energies in units of γ_B as a function of the parameter α for the first four values of n. The K and K' valleys are shown in solid and dashed blue lines, respectively. The Landau levels of the flat band are plotted in red. (c) Low-energy dispersion about one K point for $B = 0$.

perpendicular to the plane of the crystal lattice. For this case, the low-energy Hamiltonian [11] takes the form

$$H_K = -H_{K'}^* = \gamma_B \begin{pmatrix} 0 & \cos\varphi\hat{a} & 0 \\ \cos\varphi\hat{a}^\dagger & 0 & \sin\varphi\hat{a} \\ 0 & \sin\varphi\hat{a}^\dagger & 0 \end{pmatrix}, \quad (1)$$

with γ_B a magnetic energy scale given by $\gamma_B = v_F\sqrt{2eB\hbar}$. Here $\hat{a}^\dagger$ and $\hat{a}$ are the creation and annihilation operators, respectively, that obey the usual commutation relation $[\hat{a},\hat{a}^\dagger] = 1$ and act on Fock states such that $\hat{a}^\dagger|n\rangle = \sqrt{n+1}\,|n+1\rangle$ and $\hat{a}|n\rangle = \sqrt{n}\,|n-1\rangle$. Note that α has been parametrized by $\alpha = \tan\varphi$ and the Hamiltonian has been scaled by $\cos\varphi$ for convenience [11].

In the presence of the magnetic field, the electronic states of the α-T_3 model condense into Landau levels (LLs). The dispersionless flat band has zero energy LLs with energy $\varepsilon_{n,0} = 0$ for $n = 0,2,3,\ldots$. For the conduction and valence band we have

$$\varepsilon_{n,\pm} = \pm\gamma_B\sqrt{n - \frac{1}{2} - \frac{\xi}{2}\left(\frac{1-\alpha^2}{1+\alpha^2}\right)}, \quad (2)$$

with $n = 1,2,3,\ldots$ and $\xi = \pm 1$ a valley index for the K and K' valley, respectively. Figure 1(b) depicts the LL structure of the model, as a function of the parameter α (as also shown in Ref. [11]). Note the notational difference between the indices of the α-T_3 model and that of graphene. Here the indexing begins with $n = 1$ for the conduction and valence band, in contrast to graphene, where it typically starts with $n = 0$.

The wave functions for the conduction and valence bands for the lowest state ($n = 1$) are

$$|\Psi_{\pm,1}^K\rangle = \frac{1}{\sqrt{2}}\begin{pmatrix} 0 \\ \pm\ |0\rangle \\ \quad |1\rangle \end{pmatrix}, \quad |\Psi_{\pm,1}^{K'}\rangle = \frac{1}{\sqrt{2}}\begin{pmatrix} \pm\ |1\rangle \\ 0\ \ |0\rangle \end{pmatrix}, \quad (3)$$

and

$$|\Psi_{\pm,n}^K\rangle = \frac{1}{\sqrt{2}}\begin{pmatrix} \sqrt{\frac{(n-1)\cos^2\varphi}{n-\cos^2\varphi}} & |n-2\rangle \\ \pm & |n-1\rangle \\ \sqrt{\frac{n\sin^2\varphi}{n-\cos^2\varphi}} & |n\rangle \end{pmatrix}, \quad (4)$$

$$|\Psi_{\pm,n}^{K'}\rangle = \frac{1}{\sqrt{2}}\begin{pmatrix} -\sqrt{\frac{n\cos^2\varphi}{n-\sin^2\varphi}} & |n\rangle \\ \pm & |n-1\rangle \\ -\sqrt{\frac{(n-1)\sin^2\varphi}{n-\sin^2\varphi}} & |n-2\rangle \end{pmatrix}, \quad (5)$$

in general with $n = 2,3,4,\ldots$ for the K and K' valleys, respectively. For the flat band they are

$$|\Psi_{0,0}^K\rangle = \begin{pmatrix} 0 \\ 0 \\ -|0\rangle \end{pmatrix}, \quad |\Psi_{0,0}^{K'}\rangle = \begin{pmatrix} |0\rangle \\ 0 \\ 0 \end{pmatrix}, \quad (6)$$

for $n = 0$ and

$$|\Psi^K_{0,n}\rangle = \begin{pmatrix} \sqrt{\frac{n\sin^2\varphi}{n-\cos^2\varphi}} & |n-2\rangle \\ 0 & |n-1\rangle \\ -\sqrt{\frac{(n-1)\cos^2\varphi}{n-\cos^2\varphi}} & |n\rangle \end{pmatrix}, \tag{7}$$

$$|\Psi^{K'}_{0,n}\rangle = \begin{pmatrix} \sqrt{\frac{(n-1)\sin^2\varphi}{n-\sin^2\varphi}} & |n\rangle \\ 0 & |n-1\rangle \\ -\sqrt{\frac{n\cos^2\varphi}{n-\sin^2\varphi}} & |n-2\rangle \end{pmatrix}, \tag{8}$$

for $n \geqslant 2$.

III. MAGNETO-OPTICS

The absorptive part of the magneto-optical conductivity of a system can be calculated using the Kubo formula. In the Landau level basis, the Kubo formula can be written

$$\sigma_{\alpha\beta}(\omega) = \frac{ig}{2\pi\hbar l_B^2}\sum_{LLs}\frac{f-f'}{\varepsilon'-\varepsilon}\frac{\langle\Psi|\, j_\alpha\,|\Psi'\rangle\,\langle\Psi'|\, j_\beta\,|\Psi\rangle}{\omega-(\varepsilon'-\varepsilon)+i\Gamma}, \tag{9}$$

where $\alpha,\beta = \{x,y\}$ and the summation is over all initial (unprimed) and final (primed) LLs with energy ε and wave function $|\Psi\rangle$. Here f is the Fermi factor, μ is the chemical potential, and $\omega = h\nu$ is the photon energy. Here Γ can be viewed as the scattering rate of charge carriers, g is the spin degeneracy, and $l_B = \sqrt{\frac{hc}{e|B|}}$ is a magnetic length scale. The current operator is given by $j_\alpha = -ev_F S_\alpha$ with

$$S_x = \xi\begin{pmatrix} 0 & \cos\varphi & 0 \\ \cos\varphi & 0 & \sin\varphi \\ 0 & \sin\varphi & 0 \end{pmatrix}, \tag{10}$$

$$S_y = -i\begin{pmatrix} 0 & \cos\varphi & 0 \\ -\cos\varphi & 0 & \sin\varphi \\ 0 & -\sin\varphi & 0 \end{pmatrix}. \tag{11}$$

In the limit of zero temperature and zero scattering rate, the Fermi function f can be written as a Heaviside function $\theta(\mu-\varepsilon)$. {Additionally, $\mathrm{Im}\frac{1}{\omega-(\varepsilon'-\varepsilon)+i\Gamma} \to -i\pi\delta[\omega-(\varepsilon'-\varepsilon)]$ for $\Gamma \to 0$.} In our magneto-optics calculations these delta functions are broadened by scattering Γ as $\delta(x) = \frac{1}{\pi}\frac{\Gamma}{x^2+\Gamma^2}$ where we use Γ on the order of $0.025\gamma_B$.

In order to utilize Eq. (9) to calculate the magneto-optical response of the system, we require transition matrix elements that describe the probabilities of transitions between LLs. These can be written

$$\begin{aligned}&\langle\Psi^\xi_{s,n}|S_x|\Psi^\xi_{s',n'}\rangle\langle\Psi^\xi_{s',n'}|S_x|\Psi^\xi_{s,n}\rangle \\ &\quad= f_1^{\xi,n,n',s,s'}\delta_{n',n+1} + f_2^{\xi,n,n',s,s'}\delta_{n',n-1}, \\ &\langle\Psi^\xi_{s,n}|S_x|\Psi^\xi_{s',n'}\rangle\langle\Psi^\xi_{s',n'}|S_y|\Psi^\xi_{s,n}\rangle \\ &\quad= -i\left(\xi f_1^{\xi,n,n',s,s'}\delta_{n',n+1} - \xi f_2^{\xi,n,n',s,s'}\delta_{n',n-1}\right),\end{aligned} \tag{12}$$

where $f_1^{\xi,n,n',s,s'}$ and $f_2^{\xi,n,n',s,s'}$ are overlap functions between initial (unprimed) and final (primed) states where $\xi = \pm$ for the K and K' valleys, respectively; $s = \pm1,0$ for the conduction, valence, and flat band, respectively; and n, n' is the LL index. The overlap functions can be written

$$\begin{aligned} f_1^{\xi,n,n',s,s'} &= \frac{n}{4g_1(n)}[g_2(n) + 2ss'C\sqrt{g_1(n)}], \\ f_1^{\xi,n,n',0,s'} &= \frac{C}{2}\left(1 - \frac{\frac{1}{2}[1-\xi\cos(2\varphi)]}{n-\frac{1}{2}[1+\xi\cos(2\varphi)]}\right), \\ f_2^{\xi,n,n',0,s'} &= \frac{C}{2}\left(1 + \frac{\frac{1}{2}[1+\xi\cos(2\varphi)]}{n-\frac{1}{2}[1+\xi\cos(2\varphi)]}\right), \\ f_{1,2}^{\xi,n,n',0,0} &= 0, \end{aligned} \tag{13}$$

where $g_1(n) = n^2 - \xi n\cos(2\varphi) - C$, $g_2(n) = n(1-2C) + \xi\cos(2\varphi)(C-1)$, $C = \sin^2\varphi\cos^2\varphi = \frac{\alpha^2}{(1+\alpha^2)^2}$, and $s,s' = \pm$, with all cases of $s,s' = 0$ explicitly shown. The remaining overlap functions can be obtained from $f_2^{\xi,n,n',s,s'} = f_1^{\xi,n',n,s',s}$ for the cone-to-cone transitions and $f_1^{\xi,n,n',0,s'} = f_2^{\xi,n',n,s',0}$ and $f_2^{\xi,n,n',0,s'} = f_1^{\xi,n',n,s',0}$ for the flat band-to-cone transitions. The f_1 and f_2 functions give the amplitudes for the selection rules of $\delta_{n',n+1}$ and $\delta_{n',n-1}$, respectively. These amplitudes are a result of evaluating matrix elements for the inter-LL transitions which are dipole allowed. They will be uniquely activated in the presence of right-handed polarized and left-handed polarized light, respectively. For $\alpha = 0,1$ we recover the overlap functions for graphene and the dice model, respectively.

In Fig. 2 we plot the overlap functions of Eq. (13) for an intermediate value of the parameter α ($\alpha = 0.75$). We find that the f_2 overlap functions are in general greater in magnitude than the f_1 functions for flat band-to-cone transitions. For cone-to-cone interband transitions the f_1 and f_2 functions in the K' valley are dominant over their K-valley counterparts. The opposite is true for the flat band-to-cone overlap functions.

For large n, the overlap functions f_1 and f_2 approach the same limit. In particular they approach

$$\begin{aligned} f_1^{c-c} &= f_2^{c-c} = \frac{1}{4}[1 + 2C(s_1s_2 - 1)], \\ f_1^{f-c} &= f_2^{f-c} = \frac{C}{2} \end{aligned} \tag{14}$$

for cone-to-cone and flat band-to-cone transitions, respectively. Since $C(\alpha)$ is a strictly increasing function of α [see inset (c) in Fig. 2], Eq. (14) suggests that flat band-to-cone transitions become more important for $\alpha \to 1$. The opposite is true for interband cone-to-cone transitions where $s_1s_2 = -1$ and the overlap functions approach the limit $\frac{1}{4} - C(\alpha)$. The relative magnitudes of the cone-to-cone versus flat band-to-cone overlap functions in the K versus K' valley in part determine the relative peak sizes in the magneto-optics curves we will be presenting in the remainder of this section.

The absorptive diagonal component of the optical conductivity $\mathrm{Re}\,\sigma_{xx}(\omega)$ and the absorptive off-diagonal component of the optical conductivity $\mathrm{Im}\,\sigma_{xy}(\omega)$ can be calculated from the Kubo formula in Eq. (9). Additionally, for right- and left-hand polarized light, we can calculate the absorptive optical conductivity as $\mathrm{Re}\,\sigma_\pm(\omega) = \mathrm{Re}\,\sigma_{xx}(\omega) \mp \mathrm{Im}\,\sigma_{xy}(\omega)$, respectively.

We will use the notation $T_{n_s,n'_{s'}}$ to denote transitions originating from a LL with index n_s and terminating at a LL with index $n'_{s'}$. Primed and unprimed transitions T and T' will denote transitions in the K and K' valleys, respectively.

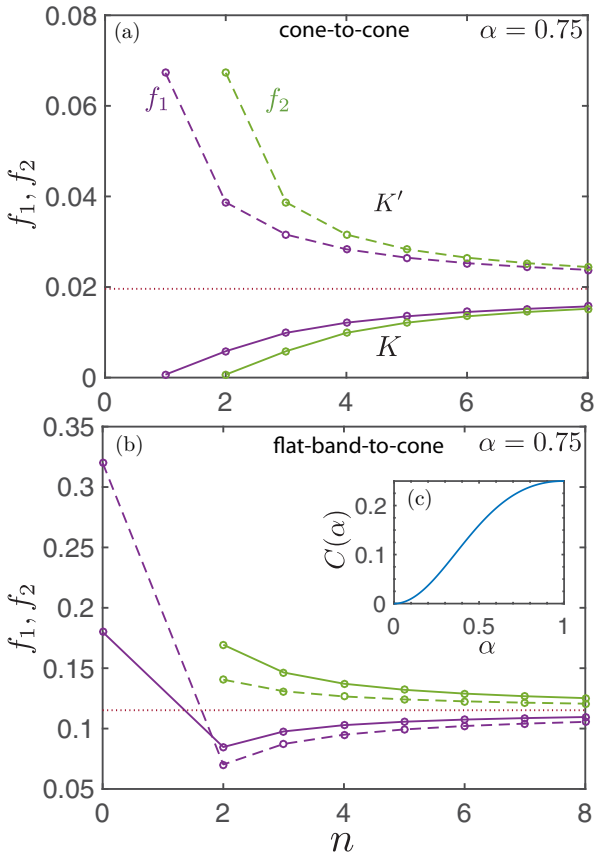

FIG. 2. (a) Cone-to-cone interband and (b) flat band-to-cone overlap functions as a function of Fock number n for $\alpha = 0.75$. Overlap functions f_1 and f_2 are shown in purple and green, respectively. The large n limit of these functions is given by Eq. (14) and denoted by a dotted red line in (a) at $C/2$ and in (b) at $1/4 - C$. Here $C = 0.2304$. The K- and K'-valley components of the overlap functions are denoted by solid and dashed lines, respectively which are simply a guide to the eye as only the values at integer n apply. In the inset (c) we show $C(\alpha)$.

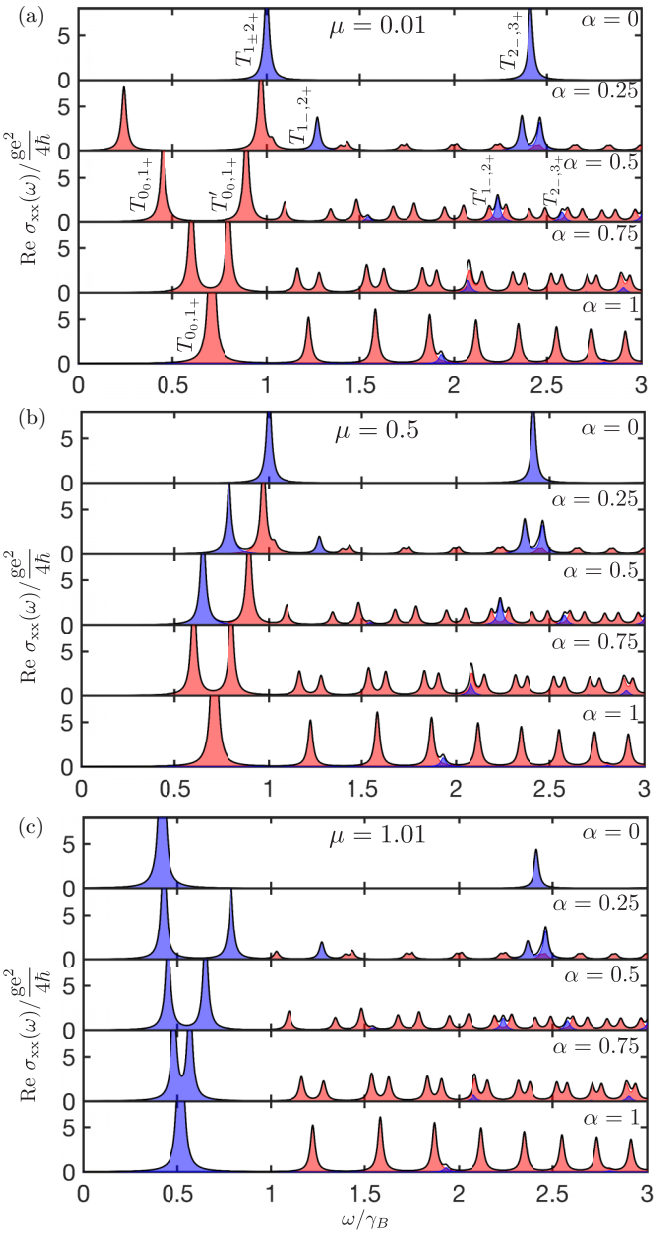

FIG. 3. Absorptive, longitudinal component of the optical conductivity $[\sigma_{xx}(\omega)]$ for a chemical potential of (a) $\mu = 0.01\gamma_B$, (b) $\mu = 0.5\gamma_B$, and (c) $\mu = 1.01\gamma_B$ for a range of α values as shown. The flat band-to-cone contributions are shaded red, while the cone-to-cone contributions are shaded blue. Their sum is shown with a thin black curve. Calculations are done using a scattering rate of $\Gamma = 0.025\gamma_B$.

For example, a transition between the first LL of the flat band ($n = 0$) and the first LL in the conduction band ($n = 1$) in the K' valley would be written $T'_{0_0,1_+}$. Note that for flat band-to-cone transitions, the energy of the transition $T_{(n+1)_0,n_+}$ is equal to that of $T_{(n-1)_0,n_+}$ and for cone-to-cone transitions, the energy of the transition $T_{(n-1)_-,n_+}$ is equal to that of $T_{n_-,(n-1)_+}$. For simplicity, we will label peaks resulting from two equal energy transitions using only one of these transitions, unless a distinction needs to be made for our purposes. Note also that for $\alpha = 0, 1$, all transitions have the same energy as their primed counterparts (i.e., $T_{n,n'} = T'_{n,n'}$). Additionally, there is no $n = 1$ LL for the flat band, and as a result there are no transitions originating from this LL.

In Fig. 3(a) we plot the absorptive diagonal component of the optical conductivity for a range of α values. They are calculated at a chemical potential $\mu = 0.1\gamma_B$, such that the smallest positive LL is above the chemical potential, and the zero energy flat band is below the chemical potential, for all values of α considered. Cone-to-cone transitions are shaded blue, and flat band-to-cone transitions are shaded red. A thin black line shows the total optical response of the system. Note again that the indexing for the LLs of the conduction and valence band of the α-T_3 model begin with $n = 1$, in contrast to the usual $n = 0$ lowest LL of graphene, which results in LL labeling that differs from what is typical for graphene.

For $\alpha = 0$ we find only cone-to-cone transitions, as expected for graphene. For the other limiting case of $\alpha = 1$, the flat band-to-cone transitions dominate, and the cone-to-cone transitions are largely suppressed. There remains only a comparatively small peak for transition $T_{1_-,2_+}$. This was also noted in Ref. [23] in their magneto-optics calculations for the pseudospin $S = 1$ system.

In the intermediate α regime, we observe the coexistence of cone-to-cone, and flat band-to-cone transitions, and the evolution between the two limiting cases. This regime is characterized by peaks with anomalous heights or locations that break up the regular pattern of the dominant transition type. For example, the $T'_{1_-,2_+}$ cone-to-cone transition disrupts the dominant pattern of the flat band-to-cone transitions. For $\alpha = 0.5$ this results in a triplet centered about the $T'_{1_-,2_+}$ transition, as its energy corresponds to the center of a flat band-to-cone doublet. For $\alpha = 0.75$, the presence of the transition lines up with one of the peaks from a flat band-to-cone doublet, and manifests as an anomalously sized doublet with increased weight on the low energy side.

Additionally, we also note a doubling of the number of peaks in the spectrum in the intermediate regime (both for cone-to-cone and flat band-to-cone transitions). This is a consequence of the difference in energies of the LLs in the K and K' valleys. For values of α close to 1, the doublets observed in the conductivity curves are formed by transitions with identical indices in the K and K' valley. For example, $T_{0_0,1_+}$ and $T'_{0_0,1_+}$ are flat band-to-cone doublets present for the full range of α in the intermediate regime, with varying separation between them.

In the other limit, for α close to 0, the doublets are formed by transitions with indices that differ by one in the two valleys. For example, $T'_{1_-,2_+}$ forms a doublet with $T_{2_-,3_+}$ in that limit. This is nicely illustrated in the LL diagram in Fig. 1(b), where we see that for values of α near 1, the LLs with the same index come together from the two valleys, whereas in the other limit, LLs with indices that differ by one converge ($n + 1$ from the K valley meets n from the K' valley).

In Figs. 3(b) and 3(c) we show $\sigma_{xx}(\omega)$ for two additional values of the chemical potential. For a chemical potential of $\mu = 0.5$ we see changes due to the increased chemical potential for two values of $\alpha = 0.25$ and 0.5, since the the chemical potential is above the first LL in the K valley for these cases. For $\mu = 1.01$ the chemical potential is above the first LL for all values of α in both the K and K' valleys. The appearance and disappearance of peaks with changing chemical potential in $\sigma_{xx}(\omega)$ will be addressed in more detail in the discussion related to Fig. 7 but is simply due to the Pauli blocking of transitions as levels are filled by increasing μ and the activation of intraband transitions. However, we include plots of higher μ here for completeness and in order to make it possible to understand the behavior of $\sigma_{xx}(\omega)$ as both a function of α and the chemical potential μ.

Figure 4 shows the absorptive off-diagonal component of the optical conductivity for the same parameters as Fig. 3. The two limiting cases of $\alpha = 0$ and 1 have already been discussed in the literature [23]. Here we focus on the intermediate regime of the α-T_3 lattice. As with the case of $\sigma_{xx}(\omega)$, we note a doubling of the peaks due to the splitting in the K- and K'-valley LLs. However, in contrast to the $\sigma_{xx}(\omega)$ there are both positive and negative valued peaks for $\sigma_{xy}(\omega)$. The signs of these peaks will be discussed in detail for the case of $\alpha = 0.25$ with relation to Fig. 8. Nevertheless, we include plots for a range of α values for a number of chemical potentials for completeness.

We now turn to examining the magneto-optical response of the α-T_3 lattice under a varying magnetic field, by making the magnitude of the magnetic field explicit in our calculations.

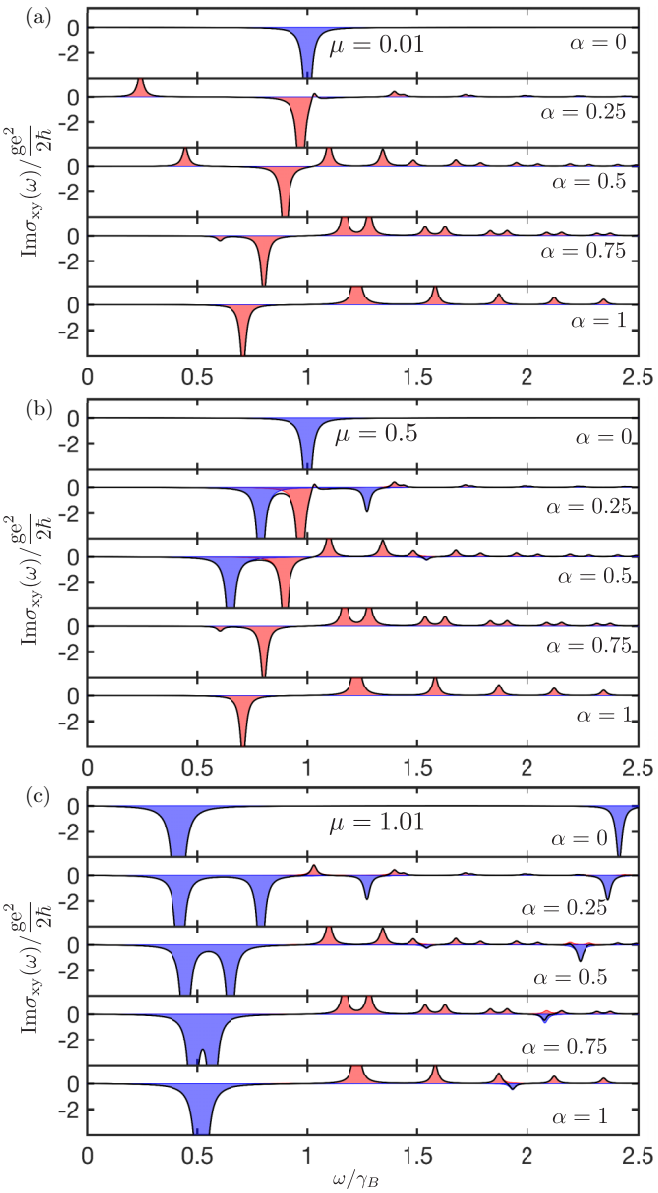

FIG. 4. Same as Fig. 3, but for the absorptive part of the transverse component of the optical conductivity [$\sigma_{xy}(\omega)$].

This allows us to connect more closely to experimental work where similar maps are an excellent tool for visualizing the LL structure and observing the magnetic field dependence of the observed transitions [17–20].

In Fig. 5 we present a false-color map of the optical conductivity as a function of the square root of the magnetic field for four values of the parameter α, including the two limiting cases of graphene and the dice lattice. As one might expect from Eq. (2), all of the observed transition energies depend on the applied magnetic field as $\sqrt{B}$ for all values of α, with slopes that depend on the value of the parameter α and the LL index n. We see the dominant cone-to-cone transition $T_{1_\pm,2_+}$ for $\alpha = 0$ and the dominant flat band-to-cone transition $T_{0_0,1_+}$ for $\alpha = 1$. These are followed by additional transitions that decrease in intensity and become more tightly spaced with increasing n.

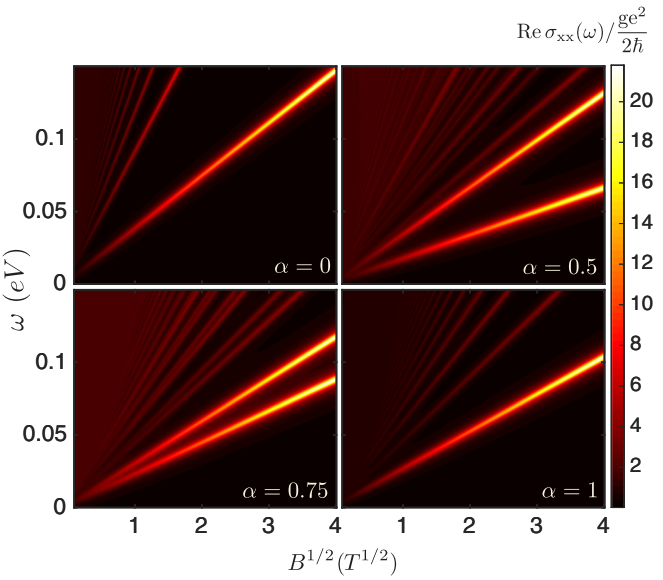

FIG. 5. Absorptive, longitudinal component of the optical conductivity under magnetic fields up to 16 T, for $\alpha = 0, 0.5, 0.75, 1$. We used a scattering rate of $\Gamma = 2.5$ meV and a chemical potential that falls below the first positive valued Landau level for all values of α considered.

For $\alpha = 0.5$ and 0.75 we see additional structure in the spacing of transitions—in the form of doublets reminiscent of those in Fig. 3. In particular, the peak associated with the $T_{0_0,1_+}$ transition is split into its K- and K'-valley counterparts and as a result, appears as two transitions of comparable intensity in this regime. The overall doublet structure of the transitions is most apparent in the $\alpha = 0.75$ color map, where we can clearly see the pattern continue even for higher energy transitions.

Next, we examine the magneto-optical response of the α-T_3 lattice as a function of the chemical potential μ. We chose a value of the coupling parameter α such that both cone-to-cone and flat band-to-cone transitions are well represented in our calculations. As can be seen in Fig. 3, $\alpha = 0.25$ is an excellent representative case.

In Fig 6 we present a snowshoe diagram [23] for $\alpha = 0.25$. Arrows represent transitions between LL, which are depicted as open circles connected by dashed and dotted lines in the K and K' valleys, respectively. The transitions shown are for a chemical potential of $\mu = 0.1\gamma_B$. Other chemical potentials of interest are also depicted in Fig. 6(a) as horizontal dashed lines, specifically $0.5\gamma_B$, $1.0\gamma_B$, $1.2\gamma_B$. These values were chosen such that for the lowest value of μ, all positive LLs are above the chemical potential and for each successive value, μ is shifted past exactly one LL, either in the K or K' valley.

In Figs. 7 through 10 we present the magneto-optical conductivity curves for $\alpha = 0.25$ including the absorptive part of the diagonal and the off-diagonal conductivities, $\mathrm{Re}\,\sigma_{xx}(\omega)$ and $\mathrm{Im}\,\sigma_{xy}(\omega)$; as well as the absorptive part of the conductivities for left- and right-hand polarized light, $\mathrm{Re}\,\sigma_+(\omega)$ and $\mathrm{Re}\,\sigma_-(\omega)$, respectively. In these figures vertical lines depict the photon energies of a number of transitions of interest. The red, blue, and green vertical lines represent the energies of flat band-to-cone transitions, cone-to-cone interband transitions, and cone-to-cone intraband transitions,

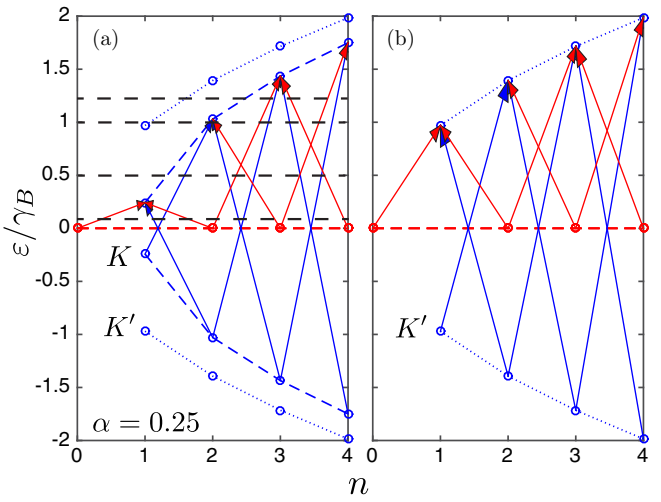

FIG. 6. Snowshoe diagram [23] for $\alpha = 0.25$. (a) Relative positions of LLs in the K and K' valleys are shown with open blue circles connected by dashed and dotted lines, respectively. Horizontal dashed lines show the four chemical potentials considered in Figs. 7 to 10. Arrows represent possible transitions between LLs in the K valley, assuming a chemical potential of $\mu = 0.1\gamma_B$. (b) LL in the K' valley with arrows depicting all possible transitions for $\mu = 0.1\gamma_B$.

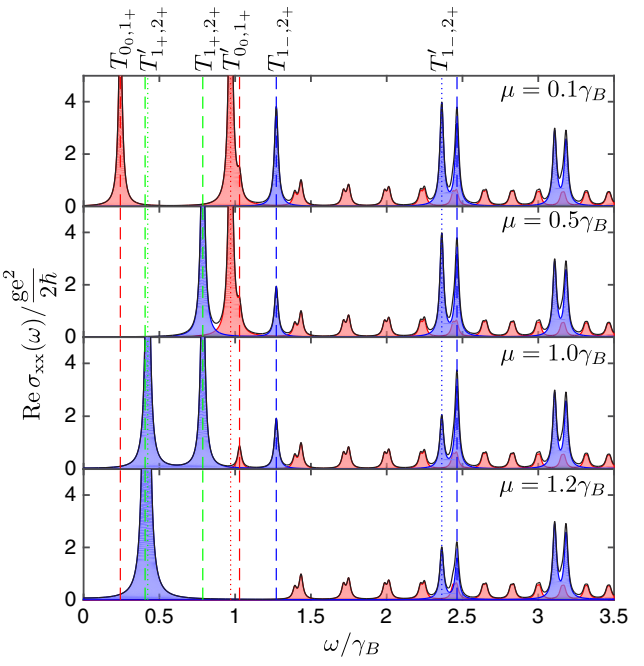

FIG. 7. Absorptive, diagonal component of the optical conductivity for $\alpha = 0.25$ showing $\mu/\gamma_B = 0.1$, 0.5, 1.0, and 1.2 from top to bottom, respectively. The flat band-to-cone (cone-to-cone) contributions are shaded red (blue), and their sum is represented by a thin black line. Vertical dashed (dotted) lines show the energies associated with a number of transitions in the K (K') valley. Red, blue, and green vertical lines mark the energy of flat band-to-cone, cone-to-cone interband, and cone-to-cone intraband transitions, respectively. In order from left to right, the following transitions are marked: $T_{0_0,1_+}$, $T_{2_+,3_+}$, $T'_{1_+,2_+}$, $T_{1_+,2_+}$, $T'_{0_0,1_+}$, $T_{1_0,2_+}$, $T_{1_-,2_+}$, $T'_{1_-,2_+}$, $T_{2_-,3_+}$. Only a subset of these are labeled above the plot.

respectively. Transitions in the K and K' valleys are shown with dashed and dotted lines, respectively. The subset of peaks that are affected by the first two shifts in chemical potential are labeled by representative transitions above the plots. We shade the flat band-to-cone response red, the cone-to-cone response blue, and denote the total optical response with a thin black curve.

In Fig. 7 we examine the effect of shifting the chemical potential past the three lowest LLs of the $\alpha = 0.25$ conductivity curve of Fig. 3. Upon increasing the chemical potential above the first LL in the K valley, a single red peak disappears, a blue peak is halved, and a new blue peak appears at an energy between the two original peaks. Similarly, raising the chemical potential above the first LL in the K' valley results in the disappearance of a red peak, the halving of a blue peak, and the appearance of a new blue peak—this time at a lower energy than either of the original transitions.

In both cases, the red peak that disappears is the lowest energy flat band-to-cone transition ($T_{0_0,1_+}$ and $T'_{0_0,1_+}$) for the respective valleys, the blue peak that is halved is the lowest energy cone-to-cone transition ($T_{1_-,2_+}$ and $T'_{1_-,2_+}$) for the respective valleys, and the transition that appears is the intraband transition that crosses the value of the chemical potential ($T_{1_+,2_+}$ and $T'_{1_+,2_+}$) for the respective valleys. Despite this, the action that takes place is not limited to the two lowest energy peaks. In fact, higher energy peaks are affected by increases in chemical potential since the lowest energy peak from a particular transition type (i.e., cone-to-cone or flat band-to-cone) is not in general the lowest energy transition in the entire spectrum.

We continue the trend in the bottom panel of Fig. 7, where the chemical potential is raised above the second LL in the K valley. We observe the disappearance of a red peak, and the disappearance of the second half of a blue peak. The intraband transition that previously appeared is also replaced by one that crosses the current value of the chemical potential (i.e., the transition $T_{1_+,2_+}$ is replaced by $T_{2_+,3_+}$). As in the previous two shifts in μ, peaks other the lowest energy ones are affected.

In contrast, for both graphene and the dice lattice, shifting the chemical potential past a single LL results in the halving or disappearance of the lowest energy cone-to-cone or flat band-to-cone interband transition, respectively. This may be accompanied by the disappearance of an intraband transition and the appearance of another intraband transition at a lower energy. Thus, for the limiting cases of $\alpha = 0, 1$ only the one or two lowest energy transitions are strongly affected by a shift in the chemical potential. In the hybrid system, multiple peaks are effected simultaneously, and these peaks are not in general the lowest energy peaks. Thus, the effects of an increased chemical potential on higher energy transitions can serve as a signature of the hybrid system.

We also note the difference in how peaks due to flat band-to-cone versus cone-to-cone transitions disappear. A flat band-to-cone peak disappears completely with a single increase in chemical potential, since transitions that contribute to those peaks terminate at the same LL. For cone-to-cone peaks, transitions that share the same energy terminate at LLs one index apart. This results in a halving of a peak, followed by the disappearance of the second half of the peak upon blocking the next LL via another increase in chemical potential. This difference between the response of cone-to-cone versus flat band-to-cone peaks to increases in chemical potential introduces additional richness into the intermediate regime. In this regime, some peaks vanish with a single shift of μ, while others are only halved.

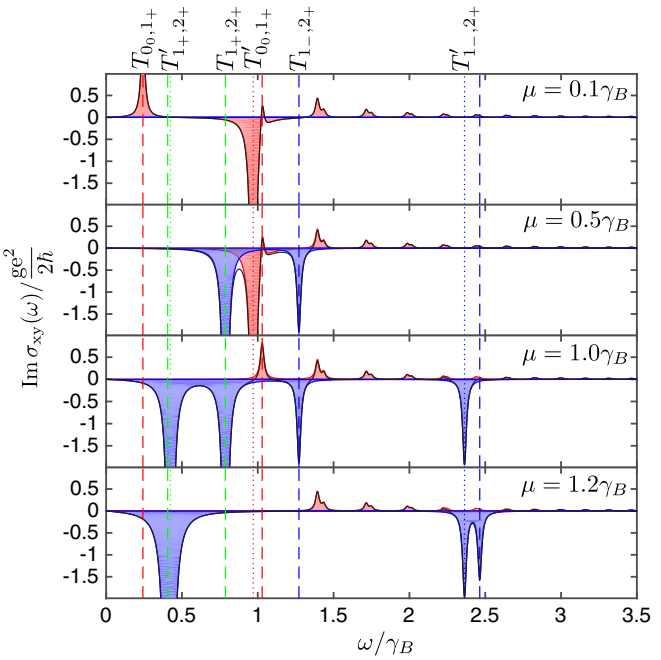

FIG. 8. Same as Fig. 7 but for the absorptive, off-diagonal component of the optical conductivity.

In Fig. 8 we plot the off-diagonal part of the absorptive optical conductivity. Here, right-directed transitions, denoted $T_{n,m}$ with $m = n + 1$, provide a negative contribution, and left-directed transitions, denoted $T_{n,m}$ with $m = n - 1$, provide a positive contribution, as can be inferred from Eq. (12). The snowshoe diagrams in Fig. 6 depicts left- and right-directed transitions as arrows that point to the left and right, respectively. The right-directed arrows are associated with the f_1 overlap functions, while the left-directed transitions are associated with the f_2 overlap functions. These different transitions can be selectively excited through right- and left-handed polarized light, which will be discussed further on. Looking at the red and blue shaded peaks, we observe that the cone-to-cone transitions behave like those of graphene and the flat band-to-cone transitions follow those of the dice lattice [23], respectively.

In particular, peaks associated with flat band-to-cone transitions in $\mathrm{Im}\,\sigma_{xy}(\omega)$ are primarily positive, due to the dominance of the left-directed (f_2) transitions. An exception is the first mixed type flat band-to-cone transition, as also seen in Ref. [23]. For cone-to-cone transitions, the overlap functions f_1 and f_2 cancel in pairs where $f_1(n)$ is paired with $f_2(n + 1)$ [see Fig. 2(a) for an example of $f_1(n) = f_2(n + 1)$]. As a result, cone-to-cone peaks only appear at energies at which one of the paired transitions is blocked. In a snowshoe diagram these transitions appear as unpaired arrows (see Fig. 6 with $\mu = 0.5$ for example). These unpaired arrows are right directed with magnitudes given by the f_1 overlap functions and are associated with negative peaks in $\mathrm{Im}\,\sigma_{xy}(\omega)$.

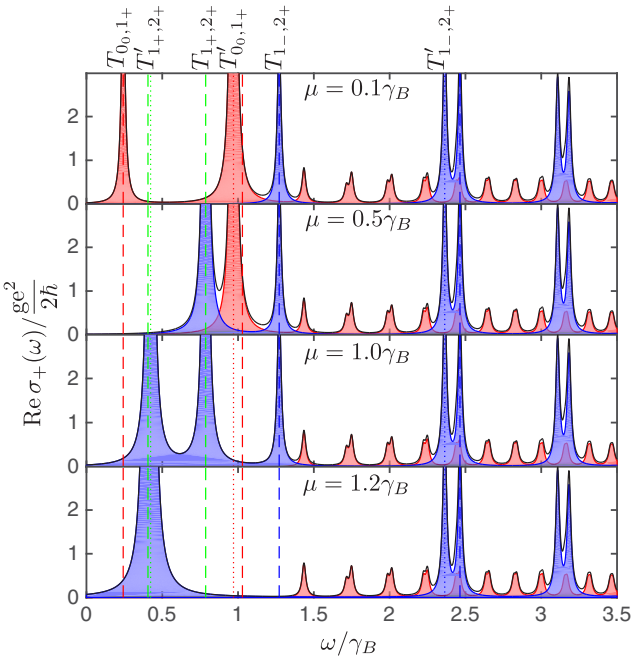

FIG. 9. Same as Fig. 7 but for the absorptive, optical conductivity for right-hand polarized light.

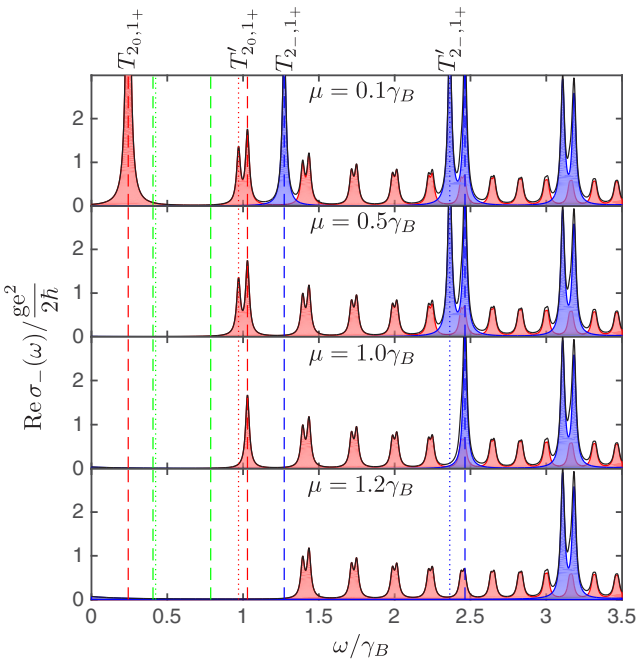

FIG. 10. Same as Fig. 7 but for the absorptive, optical conductivity for left-hand polarized light. The labels on the top have been changed to emphasize left-directed transitions.

The off-diagonal conductivity exhibits some unique features that are not present in the two limiting cases. For chemical potentials above the lowest LL, there are twice as many negative peaks from cone-to-cone transitions as there were in the $S = 1/2$ case, resulting from the difference in energies of the LLs in the K and K' valleys. This is notable as the number of peaks for $S = 1/2$ is exactly two (see Fig. 5 in Ref. [23]), and for the α-T_3 model is exactly four. Finally, we note the presence of a series of both positive and negative valued peaks which persist for larger values of chemical potential. In contrast, graphene has only negative valued peaks, while the dice lattice exhibits a single negative valued peak followed by a series of positive ones.

In Figs. 9 and 10 we plot the absorptive part of the optical conductivity for right- and left-hand polarized light, respectively. For right-hand polarized light, we find only right-directed transitions, $T_{n,m}$ with $m = n + 1$, that are associated with arrows pointing to the right in the snowshoe diagram of Fig. 6. Similarly, for left-hand polarized light we find transitions represented by left facing arrows in Fig. 6, denoted $T_{n,m}$ with $m = n - 1$. The labeling of peaks in Figs. 7 through 9 emphasizes right-directed transitions, for convenience. We reverse this labeling convention for Fig. 10, emphasizing instead the left-directed transitions that are actually visible in that figure.

For right- and left-polarized light, each peak in the conductivity curve is a result of a single transition. Consequently, cone-to-cone transitions are no longer halved before disappearing, and instead completely disappear as the chemical potential is shifted past the relevant LL. Also note that no intraband transitions exist for $\mathrm{Re}\,\sigma_-(\omega)$ since all such transitions have the form T_{n_+,m_+} with $m = n + 1$ and are only active for right-hand polarized light.

As before, in contrast to graphene and the dice lattice, we see transitions appear as doublets in the conductivity curves for polarized light. Additionally, we see peaks that are not necessarily the lowest energy interband peaks effected by a single shift in chemical potential. These are signatures of the hybrid system that persist with left- and right-hand polarized light.

As a final note, we take this opportunity to comment on the Hall conductivity of the α-T_3 model. Upon calculating the dc Hall conductivity from the Kubo formula in Eq. (9), we find that it is in agreement with our previously published results that utilized the Streda formula for this calculation [15]. Interestingly, both the flat band-to-cone and cone-to-cone contributions are required to obtain the Hall conductivity when utilizing the Kubo formula as shown in Fig. 11. In contrast, only the finite-frequency density of states was required for the same calculation using the Streda formula.

The flat-band contribution to the first nonzero valued plateau of the Hall conductivity is unique in that it can be both positive or negative valued, as shown in Fig. 11. It provides a positive contribution for values of $\alpha \approx 0.7$ or less [see Fig. 11(a)] and a negative contribution for $\alpha \approx 0.7$ or more [see Fig. 11(a)]. For all subsequent plateaux, the flat-band contribution is negative and decreases in magnitude with increasing μ.

For the case of $\alpha = 1$ we have confirmed that the relative magnitude of the flat-band contribution to the total Hall conductivity agrees with a previous analytical calculation [40]. In Ref. [41] Kovacs *et al.* calculate the Hall conductivity using Green's function's methods. Hall conductivity for the α-T_3 model is further explored in Ref. [42]. Both references find agreement with our previous calculations of the Hall conductivity [15].

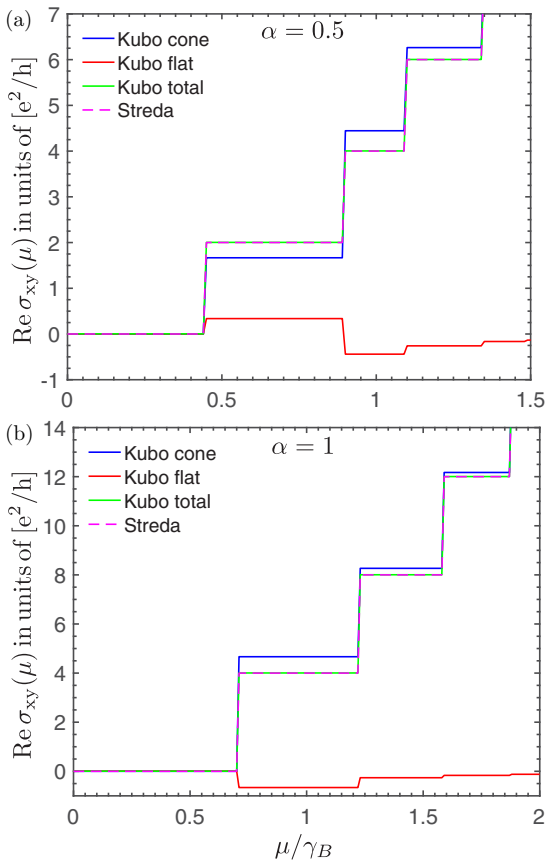

FIG. 11. DC Hall conductivity Re $\sigma_{xy}(\mu)$ for (a) $\alpha = 0.5$ and (b) $\alpha = 1$. The cone-to-cone and flat band-to-cone contributions are shown in blue and red, respectively, and their sum is shown by a green curve. We show agreement with our previously published results of the Hall conductivity that were obtained using the Streda formula in dashed magenta [15].

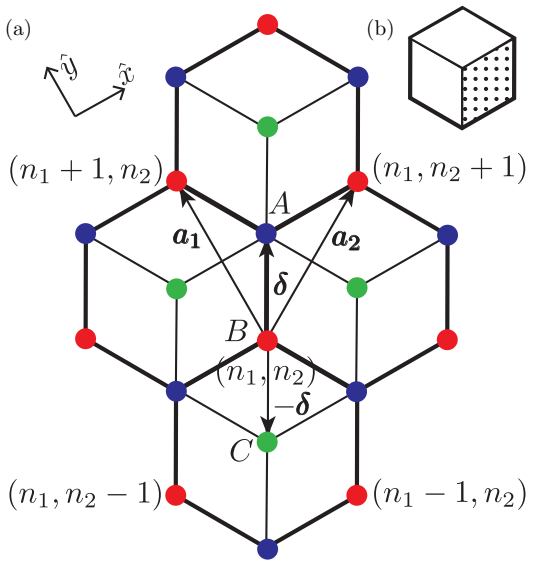

FIG. 12. (a) The α-T_3 lattice with three atoms per unit cell at sites A, B, and C, represented by blue, red, and green circles, respectively. Primitive lattice vectors $\mathbf{a}_1$ and $\mathbf{a}_2$ and basis vector $\boldsymbol{\delta}$ are depicted by arrows originating from lattice site (n_1,n_2). (b) Schematic comparing the smallest plaquette for the α-T_3 lattice for $\alpha \neq 1$ (dotted rhombus) versus $\alpha = 1$ (the entire hexagon).

IV. HOFSTADTER BUTTERFLY

In this section we consider the α-T_3 lattice in a perpendicular magnetic field and calculate the associated Hofstadter butterfly spectrum for the lattice.

We begin by choosing primitive lattice vectors $\mathbf{a}_1 = a(0,\sqrt{3})$ and $\mathbf{a}_2 = a(\frac{3}{2},\frac{\sqrt{3}}{2})$ to span the lattice. Here a is the interatomic distance, and we have chosen the vector $\mathbf{a}_1$ such that it lies in the $\hat{y}$ direction, for convenience. We choose the B sites as our lattice points, and use the basis vector $\pm\boldsymbol{\delta} = \pm a(\frac{1}{2},\frac{\sqrt{3}}{2})$ to access the atoms at sites A and C, respectively (see Fig. 12).

To denote the location of A, B, and C atoms, we can now use the vector $\mathbf{R}_n$ which can be written in terms of the primitive lattice vectors and the basis vector as

$$\mathbf{R}_{n_1,n_2,n_3} = n_1\mathbf{a}_1 + n_2\mathbf{a}_2 + n_3\boldsymbol{\delta}. \tag{15}$$

In the Landau gauge, the magnetic field in the $\hat{z}$ direction can be written $\mathbf{A} = Bx\hat{y}$. Using the usual Peierls substitution $\hbar k \to \hbar k - e\mathbf{A}/c$, the hopping t picks up a phase $\theta_{n,m}$ in the presence of the field

$$t_{n,m} \to t_{n,m}e^{-i\theta_{n,m}}. \tag{16}$$

This phase can be calculated using

$$\theta_{n,m} = \frac{e}{\hbar c}\int_{\mathbf{R}_n}^{\mathbf{R}_m} \mathbf{A}\cdot\mathbf{dl}. \tag{17}$$

Between two arbitrary nearest neighbors located at $\mathbf{R}_n$ and $\mathbf{R}_m$ the phase is given by

$$\theta_{n,m} = \frac{\pi B}{\phi_0}(\mathbf{R}_m - \mathbf{R}_n)_y(\mathbf{R}_n + \mathbf{R}_m)_x, \tag{18}$$

where $\phi_0 = hc/e$ is the quantum flux, and the subscripts x and y refer to the x and y components of the respective vectors.

In the α-T_3 lattice, atoms at sites A and C have three nearest neighbor atoms, while those at the B sites have six nearest neighbors. We can write down three coupled difference equations for the wave functions at sites A, B, and C with indices (n_1,n_2)

$$\begin{aligned}
\varepsilon\psi^B(n_1,n_2) &= t\left[e^{-i\theta_+(n_2)}\psi^A(n_1,n_2) + e^{i\theta_+(n_2)}\psi^A(n_1-1,n_2) + \psi^A(n_1,n_2-1)\right] \\
&\quad + \alpha t\left[e^{i\theta_-(n_2)}\psi^C(n_1,n_2) + e^{-i\theta_-(n_2)}\psi^C(n_1+1,n_2) + \psi^C(n_1,n_2+1)\right], \\
\varepsilon\psi^A(n_1,n_2) &= t\left[e^{i\theta_+(n_2)}\psi^B(n_1,n_2) + e^{-i\theta_+(n_2)}\psi^B(n_1+1,n_2) + \psi^B(n_1,n_2+1)\right], \\
\varepsilon\psi^C(n_1,n_2) &= \alpha t\left[e^{-i\theta_-(n_2)}\psi^B(n_1,n_2) + e^{i\theta_-(n_2)}\psi^B(n_1-1,n_2) + \psi^B(n_1,n_2-1)\right],
\end{aligned} \tag{19}$$

where $\theta_{\pm}(n_2)$ is the phase, ε is the energy, and ϕ is the elementary flux through a plaquette of the α-T_3 lattice. We have written the acquired phase $\theta_{n,m}(n_2)$ as $\theta_{\pm}(n_2) = \pi\frac{\phi}{\phi_0}(n_2 \pm \frac{1}{6})$ in Eq. (19) for the particular set of basis vectors we have chosen for the α-T_3 lattice. Here the elementary flux $\phi = \frac{Ba^2\sqrt{3}}{2}$, where $\frac{a^2\sqrt{3}}{2}$ is the area of the smallest plaquette of the α-T_3 lattice for $\alpha \neq 0$ as depicted in Fig. 12(b). Note that we have suppressed the third index n_3 in the wave functions of Eq. (19), since n_3 is always 1, 0, and -1 for atoms at sites A, B, and C, respectively [see Eq. (15)].

Upon combining the three difference equations from Eq. (19) via substitution into the top equation one can obtain a single difference equation for $\psi^B(n_1,n_2)$ that is valid for $\varepsilon \neq 0$. Taking into account the translational symmetry in the $\hat{y}$ direction due to the gauge choice [6], we can assume plane wave behavior in this direction and look for solutions of the form

$$\psi^B(n_1,n_2) = \varphi_{n_2}e^{ik_1n_1}, \quad k_1 = \mathbf{a_1}\cdot\mathbf{k} = ak_y\sqrt{3}. \tag{20}$$

Simplification and some algebra yields a second order difference equation for φ_{n_2},

$$\begin{aligned}[\varepsilon^2 - 3t^2(1+\alpha^2)]\varphi_{n_2} = {} & 2t^2\varphi_{n_2}\left(\cos\left\{\left[6\pi\frac{\phi}{\phi_0}\left(n_2+\frac{1}{6}\right)\right]-k_1\right\}+\alpha^2\cos\left\{\left[6\pi\frac{\phi}{\phi_0}\left(n_2-\frac{1}{6}\right)\right]-k_1\right\}\right)\\ & +2t^2\varphi_{n_2-1}\left(\cos\left\{\left[3\pi\frac{\phi}{\phi_0}\left(n_2-\frac{5}{6}\right)\right]-\frac{k_1}{2}\right\}+\alpha^2\cos\left\{\left[3\pi\frac{\phi}{\phi_0}\left(n_2-\frac{1}{6}\right)\right]-\frac{k_1}{2}\right\}\right)\\ & +2t^2\varphi_{n_2+1}\left(\cos\left\{\left[3\pi\frac{\phi}{\phi_0}\left(n_2+\frac{1}{6}\right)\right]-\frac{k_1}{2}\right\}+\alpha^2\cos\left\{\left[3\pi\frac{\phi}{\phi_0}\left(n_2+\frac{5}{6}\right)\right]-\frac{k_1}{2}\right\}\right).\end{aligned} \tag{21}$$

It is easy to verify that Eq. (21) reduces to the equation for the Hofstadter butterfly for the HCL and the dice lattice in the appropriate limits [7,35] of $\alpha = 0$ and $\alpha = 1$, respectively. Rational values of $\frac{\phi}{\phi_0} = \frac{p}{q}$ make Eq. (21) periodic. Applying Bloch's theorem to take advantage of the periodicity yields a $q \times q$ eigenvalue equation for energy ε. We solve this system of q equations to obtain Hofstadter butterflies for the α-T_3 lattice.

In Fig. 13 we show the Hofstadter spectra for six representative values of α. The spectra were calculated with a q up to 50 and plotted as a function of $\frac{\phi}{\phi_0}$. The $\varepsilon = 0$ solution that results from the nondispersive flat band for all values of magnetic field is also included in the spectra though it is not given by Eq. (21). As one might expect from Eq. (21) and the symmetries of the α-T_3 lattice, the Hofstadter butterfly spectra are symmetric about $\varepsilon = 0$ and $\frac{\phi}{\phi_0} = \frac{1}{2}$, for all values of α, with additional symmetries present in the $\alpha \to 0$ limit.

For the limiting case of $\alpha = 1$, we obtain the Hofstadter butterfly spectrum of the dice lattice [see Fig. 13(f)]. The spectrum has a highly degenerate eigenvalue resulting from the presence of the flat band at $\varepsilon = 0$ that carries 1/3 of the total weight. The spectrum contains a number of gaps, for example a large circular one near the center, which at $\frac{\phi}{\phi_0} = \frac{1}{2}$ is accompanied by a collapse of all the states to just three degenerate eigenvalues of $\varepsilon = 0$ and $\varepsilon = \pm\sqrt{6}t$. There are also a number of gapless bands, for example a large one at $\frac{\phi}{\phi_0} = \frac{1}{3}$ that stretches between $\varepsilon = \pm 3t$. A more detailed discussion of the Hofstadter butterfly spectrum for the dice lattice can be found in Refs. [6,7].

For the other limiting case of $\alpha = 0$, we obtain three repeats of the Hofstadter butterfly of graphene [see Fig. 13(a)]. Focusing on a single repeat in the central region with $\frac{1}{3} < |\frac{\phi}{\phi_0}| < \frac{2}{3}$, the HCL Hofstadter butterfly is characterized by a set of gaps whose shape resembles the letter X, located at both positive and negative energies. Repeats of this shape can be found throughout the complex fractal pattern of the HCL Hofstadter butterfly. At $\frac{\phi}{\phi_0} = \frac{1}{2}$ there is a gapless band that stretches between $\varepsilon = \pm\sqrt{6}t$, in contrast to the three highly degenerate eigenvalues found for the dice lattice at the same flux.

Notably, we obtain three copies of the graphene Hofstadter butterfly spectrum, but only a single copy of the dice lattice one for the same range of $\frac{\phi}{\phi_0}$ in Fig. 13. This can be understood by looking at the diagram in Fig. 12(b) which contrasts the smallest plaquette that can be encircled by a semiclassical orbit for the HCL versus the α-T_3 lattice. Semiclassically, the smallest orbit an electron can make in the α-T_3 lattice, with $\alpha \neq 0$, is along the edges of a rhombus with vertices A, B, A, C. An example of such a rhombus is highlighted with dotted fill in Fig. 12(b). This rhombus has an area $\frac{\sqrt{3}a^2}{2}$. In contrast, for $\alpha = 0$, the atoms at the C sites are inert, and cannot be part of a semiclassical orbit. In this limit, the smallest orbit is the entire hexagon in Fig. 12(b), which contains three copies of the rhombus, resulting in an area of $\frac{3\sqrt{3}a^2}{2}$. Since $\phi = \frac{Ba^2\sqrt{3}}{2}$, where $\frac{a^2\sqrt{3}}{2}$ is the area of the smallest plaquette of the α-T_3 lattice for $\alpha \neq 0$, this results in three repeats of the Hofstadter butterfly for $\alpha = 0$, where the area of the smallest plaquette is three times larger.

As α changes from 1 to 0 we observe the Hofstadter butterfly change its periodicity by a factor of three. In the process, the large circular gap in the central region is squeezed from above and below, while the two side regions with $|\frac{\phi}{\phi_0}| > \frac{1}{3}$ symmetrically evolve to form two copies of the graphene Hofstadter butterfly spectrum. During this process, a number of striking changes take place in the spectra. Notably, at $\frac{\phi}{\phi_0} = \frac{1}{2}$, the highly degenerate eigenvalues we observe for $\alpha = 1$ evolve into a large gapless band for $\alpha = 0$. Quantitatively, the gap centered about $\frac{\phi}{\phi_0} = \frac{1}{2}$ is bounded by $\varepsilon = \pm\sqrt{6\alpha}t$. Consequently, the band at $\frac{\phi}{\phi_0} = \frac{1}{2}$ stretches from $\pm\sqrt{6\alpha}t$ to $\pm\sqrt{6}t$ resulting in highly degenerate eigenvalues at $\pm\sqrt{6}t$ for $\alpha = 1$ and a continuous band between $\pm\sqrt{6}t$ for $\alpha = 0$.

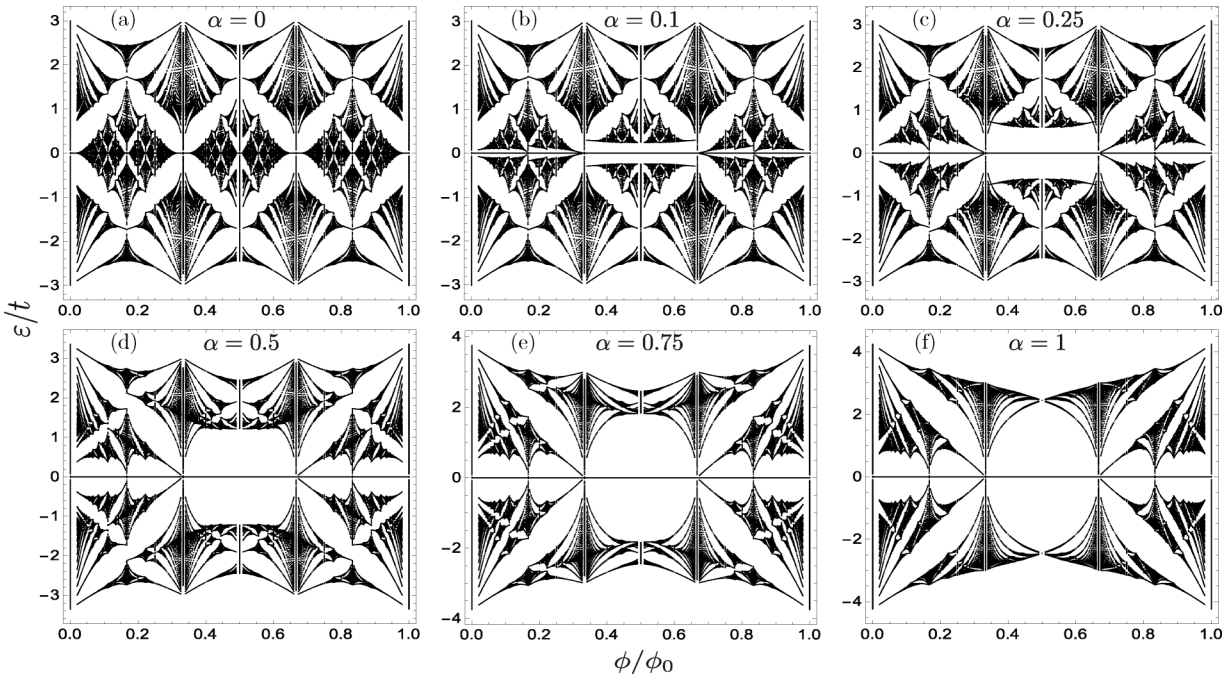

FIG. 13. Hofstadter butterflies for six representative α values calculated for q up to 50.

Recent seminal experiments in Moire superlattices have focused on observing the small field portion of the Hofstadter butterfly spectrum, since these regions are most readily accessible in the laboratory. In Fig. 14 we highlight this portion of the Hofstadter butterfly spectrum for $\alpha = 0$ and $\alpha = 0.25$, for the α-T_3 lattice. For both $\alpha = 0$ and 0.25 we see a series of electronlike LLs that move up in energy with increasing ϕ. These are the LLs given by Eq. (2) that are formed in the cones located at the K and K' points. Additionally, we see holelike LLs that move down in energy with increasing ϕ. These are accommodated in the hole pocket formed at the center of the hexagonal Brillouin zone [26].

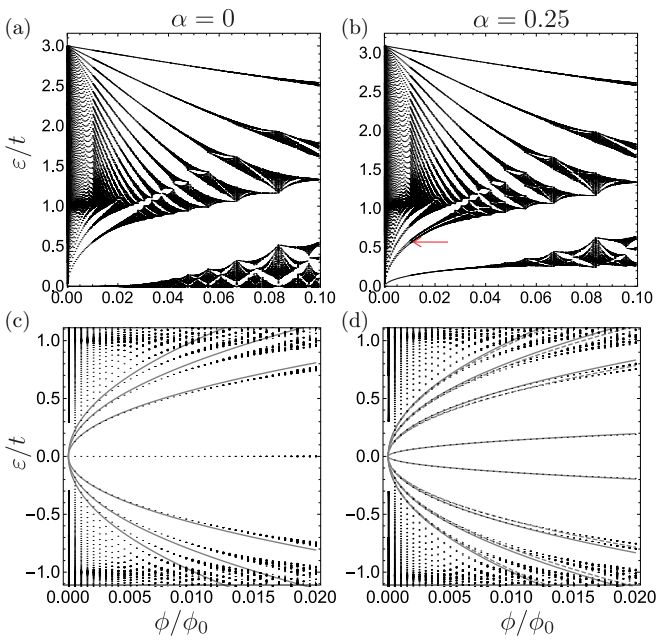

FIG. 14. Low-field Hofstadter spectra for (a) $\alpha = 0$ and (b) $\alpha = 0.25$. The red arrow in (b) highlights the splitting of the LLs that is visible in the $\alpha = 0.25$ butterfly. For very low field, bands are compared with the spectra for (c) $\alpha = 0$ and (d) $\alpha = 0.25$ with K and K' bands shown by solid and dashed lines, respectively. The low-field bands are given by Eq. (22).

For $\alpha = 0.25$, the splitting between the LLs in the K and K' valley can be observed in the LLs. This splitting is characterized by an unusually small spacing between LLs that interrupts the usual spacing observed between the remainder of the levels. An example of this is shown by the arrow in Fig. 14(b).

Quantitatively, the low-field spectra in Figs. 14(a) and 14(b) can be described by bands with energy

$$\varepsilon_n\left(\frac{\phi}{\phi_0}\right) = \pm 3t\sqrt{\frac{2\pi}{\sqrt{3}}}\sqrt{n - \frac{1}{2} - \frac{\xi}{2}\left(\frac{1-\alpha^2}{1+\alpha^2}\right)}\sqrt{\frac{\phi}{\phi_0}}. \quad (22)$$

These bands are shown in Figs. 14(c) and 14(d) for $\alpha = 0$ and 0.25, respectively, and show the splitting between the LL of the K and K' valley in more detail.

As the possibility of measuring the Hofstadter butterfly in graphenelike systems is starting to become a reality, it is appropriate to provide a characterization of this spectrum for the α-T_3 model discussed here.

V. CONCLUSIONS

In this paper we described the magneto-optical response and the Hofstadter butterfly spectrum of the α-T_3 lattice. We highlighted signatures of the intermediate regime between the pseudospin $S = 1/2$ HCL and the pseudospin $S = 1$ dice lattice.

In the magneto-optical conductivity, we noted a coexistence of the cone-to-cone transitions of graphene and flat band-to-

cone transitions of the dice lattice in the intermediate regime of the α-T_3 model. This was accompanied by a doubling of peaks associated with both transition types, a consequence of the inequivalent LL energies in the K and K' valleys. This interplay of the two transition types resulted in richness not observed in the two limiting cases, including anomalously sized peaks and doublets, as well as triplets of peaks.

Examining the magneto-optical response with a varying magnetic field B showed $\sqrt{B}$ dependence for all transitions. In the intermediate regime, a doublet structure in the peaks was again apparent, and in this case was manifest as pairs of transitions with comparable intensity.

For the HCL and the dice lattice, varying the chemical potential primarily affects the lowest energy transitions of the magneto-optical conductivity curves. In the intermediate regime of the α-T_3 model, this action is not limited to the lowest energy peaks due to the richness of the mixing of cone-to-cone and flat band-to-cone transitions.

We confirm here that our DC quantized Hall conductance calculated from the $\omega = 0$ limit of the Kubo formula is in agreement with our previous calculation [15] using the Streda formula. While the Streda formula only uses the finite frequency density of states, the Kubo approach required both cone-to-cone transitions and flat band-to-cone transitions, although the latter are a minor contribution. An interesting result is that the flat band-to-cone contribution to the first finite plateau of the Hall conductance shows anomalous behavior as a function of α with a change in sign around $\alpha \approx 0.7$. We note that in the α-T_3 model, the susceptibility was found to show a transition from diamagnetic to paramagnetic behavior as α was varied from 0 to 1 with the change occurring for $\alpha \approx 0.52$ [11]. It is possible that the sign change we find might be related. Further investigation into other features of the α-T_3 model which could exhibit such sign changes with α might be of interest in light of these findings.

Finally, we derived the difference equation required to calculate the Hofstadter butterfly spectrum for the intermediate regime of the α-T_3 lattice. This allowed us to describe the evolution of the Hofstadter spectrum as it changes its period by a factor of three. Also, we highlighted the low-field regime of the Hofstadter spectrum, as this is the regime most accessible for recent experiments in other lattices.

ACKNOWLEDGMENTS

We acknowledge J. P. Carbotte, G. Demand, and J. D. Malcolm for useful discussions. This work has been supported by the Natural Sciences and Engineering Research Council (NSERC) of Canada.

[1] K. S. Novoselov, A. K. Geim, S. V. Morozov, D. Jiang, Y. Zhang, S. V. Dubonos, I. V. Grigorieva, and A. A. Firsov, Electric field effect in atomically thin carbon films, Science **306**, 666 (2004).

[2] J. W. McClure, Diamagnetism of graphite, Phys. Rev. **104**, 666 (1956).

[3] Y. Zheng and T. Ando, Hall conductivity of a two-dimensional graphite system, Phys. Rev. B **65**, 245420 (2002).

[4] V. P. Gusynin and S. G. Sharapov, Unconventional Integer Quantum Hall Effect in Graphene, Phys. Rev. Lett. **95**, 146801 (2005).

[5] Y. Zhang, Y.-W. Tan, H. L. Stormer, and P. Kim, Experimental observation of the quantum Hall effect and Berry's phase in graphene, Nature (London) **438**, 201 (2005).

[6] J. Vidal, P. Butaud, B. Douçot, and R. Mosseri, Disorder and interactions in Aharonov-Bohm cages, Phys. Rev. B **64**, 155306 (2001).

[7] J. Vidal, R. Mosseri, and B. Douçot, Aharonov-Bohm Cages in Two-Dimensional Structures, Phys. Rev. Lett. **81**, 5888 (1998).

[8] B. Dóra, J. Kailasvuori, and R. Moessner, Lattice generalization of the Dirac equation to general spin and the role of the flat band, Phys. Rev. B **84**, 195422 (2011).

[9] F. Wang and Y. Ran, Nearly flat band with Chern number $c = 2$ on the dice lattice, Phys. Rev. B **84**, 241103 (2011).

[10] D. Bercioux, D. F. Urban, H. Grabert, and W. Häusler, Massless Dirac-Weyl fermions in a $\mathcal{T}_3$ optical lattice, Phys. Rev. A **80**, 063603 (2009).

[11] A. Raoux, M. Morigi, J.-N. Fuchs, F. Piéchon, and G. Montambaux, From Dia- to Paramagnetic Orbital Susceptibility of Massless Fermions, Phys. Rev. Lett. **112**, 026402 (2014).

[12] J. D. Malcolm and E. J. Nicol, Magneto-optics of massless Kane fermions: Role of the flat band and unusual berry phase, Phys. Rev. B **92**, 035118 (2015).

[13] T. Louvet, P. Delplace, A. A. Fedorenko, and D. Carpentier, On the origin of minimal conductivity at a band crossing, Phys. Rev. B **92**, 155116 (2015).

[14] F. Piéchon, J.-N. Fuchs, A. Raoux, and G. Montambaux, Tunable orbital susceptibility in α-T_3 tight-binding models, J. Phys.: Conf. Ser. **603**, 012001 (2015).

[15] E. Illes, J. P. Carbotte, and E. J. Nicol, Hall quantization and optical conductivity evolution with variable Berry phase in the α-T_3 model, Phys. Rev. B **92**, 245410 (2015).

[16] M. Orlita and M. Potemski, Dirac electronic states in graphene systems: Optical spectroscopy studies, Semicond. Sci. Technol. **25**, 063001 (2010).

[17] Z. Jiang, E. A. Henriksen, L. C. Tung, Y.-J. Wang, M. E. Schwartz, M. Y. Han, P. Kim, and H. L. Stormer, Infrared Spectroscopy of Landau Levels of Graphene, Phys. Rev. Lett. **98**, 197403 (2007).

[18] R. S. Deacon, K.-C. Chuang, R. J. Nicholas, K. S. Novoselov, and A. K. Geim, Cyclotron resonance study of the electron and hole velocity in graphene monolayers, Phys. Rev. B **76**, 081406 (2007).

[19] M. L. Sadowski, G. Martinez, M. Potemski, C. Berger, and W. A. de Heer, Landau Level Spectroscopy of Ultrathin Graphite Layers, Phys. Rev. Lett. **97**, 266405 (2006).

[20] P. Plochocka, C. Faugeras, M. Orlita, M. L. Sadowski, G. Martinez, M. Potemski, M. O. Goerbig, J.-N. Fuchs, C. Berger, and W. A. de Heer, High-Energy Limit of Massless Dirac Fermions in Multilayer Graphene using Magneto-optical Transmission Spectroscopy, Phys. Rev. Lett. **100**, 087401 (2008).

[21] N. H. Shon and T. Ando, Quantum transport in two-dimensional graphite system, J. Phys. Soc. Jpn. **67**, 2421 (1998).
[22] M. Koshino and T. Ando, Magneto-optical properties of multilayer graphene, Phys. Rev. B **77**, 115313 (2008).
[23] J. D. Malcolm and E. J. Nicol, Magneto-optics of general pseudospin-s two-dimensional Dirac-Weyl fermions, Phys. Rev. B **90**, 035405 (2014).
[24] D. R. Hofstadter, Energy levels and wave functions of Bloch electrons in rational and irrational magnetic fields, Phys. Rev. B **14**, 2239 (1976).
[25] G. Gumbs, A. Iurov, D. Huang, and L. Zhemchuzhna, Revealing Hofstadter spectrum for graphene in a periodic potential, Phys. Rev. B **89**, 241407 (2014).
[26] P. Moon and M. Koshino, Energy spectrum and quantum Hall effect in twisted bilayer graphene, Phys. Rev. B **85**, 195458 (2012).
[27] R. Bistritzer and A. H. MacDonald, Moiré butterflies in twisted bilayer graphene, Phys. Rev. B **84**, 035440 (2011).
[28] Z. F. Wang, F. Liu, and M. Y. Chou, Fractal Landau-level spectra in twisted bilayer graphene, Nano Lett. **12**, 3833 (2012).
[29] C. R. Dean, L. Wang, P. Maher, C. Forsythe, F. Ghahari, Y. Gao, J. Katoch, M. Ishigami, P. Moon, M. Koshino, T. Taniguchi, K. Watanabe, K. L. Shepard, J. Hone, and P. Kim, Hofstadter's butterfly and the fractal quantum hall effect in moire superlattices, Nature (London) **497**, 598 (2013).
[30] G. L. Yu, R. V. Gorbachev, J. S. Tu, A. V. Kretinin, Y. Cao, R. Jalil, F. Withers, L. A. Ponomarenko, B. A. Piot, M. Potemski, D. C. Elias, X. Chen, K. Watanabe, T. Taniguchi, I. V. Grigorieva, K. S. Novoselov, V. I. Fal'ko, A. K. Geim, and A. Mishchenko, Hierarchy of Hofstadter states and replica quantum Hall ferromagnetism in graphene superlattices, Nat. Phys. **10**, 525 (2014).
[31] L. A. Ponomarenko, R. V. Gorbachev, G. L. Yu, D. C. Elias, R. Jalil, A. A. Patel, A. Mishchenko, A. S. Mayorov, C. R. Woods, J. R. Wallbank, M. Mucha-Kruczynski, B. A. Piot, M. Potemski, I. V. Grigorieva, K. S. Novoselov, F. Guinea, V. I. Fal'ko, and A. K. Geim, Cloning of Dirac fermions in graphene superlattices, Nature (London) **497**, 594 (2013).
[32] B. Hunt, J. D. Sanchez-Yamagishi, A. F. Young, M. Yankowitz, B. J. LeRoy, K. Watanabe, T. Taniguchi, P. Moon, M. Koshino, P. Jarillo-Herrero, and R. C. Ashoori, Massive Dirac fermions and Hofstadter butterfly in a van der Waals heterostructure, Science **340**, 1427 (2013).
[33] M. Aidelsburger, M. Atala, M. Lohse, J. T. Barreiro, B. Paredes, and I. Bloch, Realization of the Hofstadter Hamiltonian with Ultracold Atoms in Optical Lattices, Phys. Rev. Lett. **111**, 185301 (2013).
[34] H. Miyake, G. A. Siviloglou, C. J. Kennedy, W. C. Burton, and W. Ketterle, Realizing the Harper Hamiltonian with Laser-Assisted Tunneling in Optical Lattices, Phys. Rev. Lett. **111**, 185302 (2013).
[35] R. Rammal, Landau level spectrum of Bloch electrons in a honeycomb lattice, J. Phys. France **46**, 1345 (1985).
[36] F. H. Claro and G. H. Wannier, Magnetic subband structure of electrons in hexagonal lattices, Phys. Rev. B **19**, 6068 (1979).
[37] G. Gumbs and P. Fekete, Hofstadter butterfly for the hexagonal lattice, Phys. Rev. B **56**, 3787 (1997).
[38] M. Kohmoto and A. Sedrakyan, Hofstadter problem on the honeycomb and triangular lattices: Bethe ansatz solution, Phys. Rev. B **73**, 235118 (2006).
[39] P. Dietl, F. Piéchon, and G. Montambaux, New Magnetic Field Dependence of Landau Levels in a Graphenelike Structure, Phys. Rev. Lett. **100**, 236405 (2008).
[40] J. D. Malcolm (private communication).
[41] Á. D. Kovács, G. Dávid, B. Dóra, and J. Cserti, Frequency dependent magneto-optical conductivity in the generalized α-T_3 model, arXiv:1605.09588.
[42] T. Biswas and T. Kanti Ghosh, Magnetotransport properties of the α-T_3 model, arXiv:1605.06680.